

Laser-annealing Josephson junctions for yielding scaled-up superconducting quantum processors.

Jared B. Hertzberg, Eric J. Zhang, Sami Rosenblatt, Easwar Magesan, John A. Smolin, Jeng-Bang Yau, Vivekananda P. Adiga, Martin Sandberg, Markus Brink, Jerry M. Chow, and Jason S. Orcutt
IBM Quantum, IBM T.J. Watson Research Center, Yorktown Heights, NY 10598, USA

(Dated: September 16, 2020)

As superconducting quantum circuits scale to larger sizes, the problem of frequency crowding proves a formidable task. Here we present a solution for this problem in fixed-frequency qubit architectures. By systematically adjusting qubit frequencies post-fabrication, we show a nearly ten-fold improvement in the precision of setting qubit frequencies. To assess scalability, we identify the types of ‘frequency collisions’ that will impair a transmon qubit and cross-resonance gate architecture. Using statistical modeling, we compute the probability of evading all such conditions, as a function of qubit frequency precision. We find that without post-fabrication tuning, the probability of finding a workable lattice quickly approaches 0. However with the demonstrated precisions it is possible to find collision-free lattices with favorable yield. These techniques and models are currently employed in available quantum systems and will be indispensable as systems continue to scale to larger sizes.

I. INTRODUCTION

Realizing robust large-scale quantum information processors is one of the foremost challenges in quantum science. Many practical applications have been proposed for robust quantum computers, including estimating the ground state energy of chemical compounds and implementing machine learning algorithms [1–5]. Quantum advantage relative to classical computers can be realized without full fault-tolerance, but requires large quantum circuits that a classical computer cannot simulate [6]. Recent demonstrations have shown qubit circuits nearly at the threshold for demonstrating quantum advantage [7]. Much work remains in order to realize fault-tolerant quantum processors; however, scale-up of solid-state quantum circuits has shown consistent and ongoing progress [8–15]. As the qubit circuits are scaled up, they must maintain high one- and two-qubit gate fidelities, high qubit connectivity, and low cross-talk error which can be measured in a holistic sense via the quantum volume of the circuit [16]. Lattices of fixed-frequency transmon qubits represent a promising architecture for building systems of larger sizes [7]. A growing number of systems at the 20 to 50-qubit scale are now available to users through cloud access. A variety of technical challenges confront further system scaling, including improving 3-dimensional circuit integration and qubit coherence. High on the list of such challenges is the issue of ‘frequency crowding.’

Fixed frequency transmon qubits using the two-qubit cross-resonance (CR) gate form a promising architecture for scaling up quantum systems. Fixed-frequency transmons are largely insensitive to charge or flux noise, and have achieved coherence times of 100 μ s and growing. The CR gate, a hardware-efficient all-microwave gate [17–20], is readily used to entangle these qubits with gate fidelities above 99%, approaching the threshold for fault-tolerant codes [21]. To achieve these fidelities, the CR gate needs not only high coherence qubits, but also a precise setting of the qubits’ frequencies. The CR gate

activates a ZX interaction by driving one ‘control’ qubit with a microwave pulse at the other ‘target’ qubit’s transition frequency. The magnitude of the ZX as well as other Hamiltonian terms depends on the relative frequencies of the two qubits [22, 23]. Diminished ZX magnitude increases gate time, while other terms such as ZZ add gate errors. Neighboring qubits having the wrong detuning will exhibit a ‘frequency collision’ in which the ZX may be suppressed or other undesirable effects arise.

Maintaining high gate fidelities for all pairs in a lattice will require solving this ‘frequency crowding’ problem by precise setting of qubit frequencies to specified values, as characterized by a standard deviation σ_f . To achieve low σ_f , the tunnel-junction conductance must be controlled with high precision. Transmon frequency f_{01} follows $hf_{01} \simeq \sqrt{8E_J E_C} - E_C$, where Josephson energy $E_J = \frac{\hbar I_c}{2e}$ is many times greater than charging energy $E_C = \frac{e^2}{2C}$ [24]. In typical transmons, a photolithographically defined capacitance C has dimensions in the tens to hundreds of microns and varies little from qubit to qubit. The critical current I_c is set by a tunnel barrier of area $\sim 100 \times 100$ nm and thickness a few nm, and is thus challenging to fabricate with precision better than a few percent [25–28]. However, tunnel barrier resistance R_n is readily measurable to precision better than 0.1% and relates to I_c according to the Ambegaokar-Baratoff relation $I_c = \frac{\pi \Delta}{2e R_n}$ (where Δ is the superconducting gap energy) [29]. We can therefore measure R_n before a chip is cooled in order to assess qubit frequency imprecision. The best demonstrated precision in setting R_n at time of fabrication is 2% [28]. A 2% variation in R_n indicates a fractional σ_f of 1%.

Careful design of lattices can enable error correction codes while at the same time minimizing the likelihood of ‘frequency collisions’ and therefore the required σ_f for fabrication yield [30, 31]. Yet even the most robust designs require a fractional σ_f of 0.25% to 0.5%, which represents a factor of 2 to 4 improvement over the

best literature results. To overcome such limits will require rework of individual qubits' tunnel junctions after fabrication. Thermal anneal has been shown to increase tunnel resistance R_n , and laser heating has been demonstrated as a highly localized re-work tool [32–37]. However, the inherent variability of the anneal process itself must be overcome, and qubit frequency control utilizing such techniques at scale has never been presented in the literature.

In this paper, we introduce an adaptive post-fabrication trimming technique that we use to incrementally adjust R_n on a qubit-by-qubit basis, thereby overcoming inherent variability in both initial qubit fabrication and the laser anneal. For the first time, an improvement in qubit frequency precision is demonstrated in terms of narrowed frequency distributions. Crucially, we demonstrate qubit frequency imprecision σ_f of the same magnitude as the imprecision of predicting f_{01} from R_n . To estimate the scalability of this technique for the fabrication of error-corrected lattices, we employ a statistical yield model based on σ_f relative to specific collision bounds. This model predicts the severity of the frequency crowding problem for different topologies and scales of error corrected multi-qubit lattices as a function of code distance. The model demonstrates that using conventional transmon fabrication, scaled-up qubit lattices will fail to evade ‘frequency collisions’. However, our novel trimming technique achieves adequate σ_f for scalable fabrication of distance-3 through distance-7 heavy-square and heavy-hexagon codes. In particular, this technique enables the high yield fabrication of the distance-3 and distance-5 heavy-hexagon lattices currently deployed as IBM cloud connected systems [38].

II. RESULTS

A. Frequency Precision σ_f From Transmon Fabrication

To assess the σ_f resulting from qubit fabrication, we developed a test vehicle containing a large number of identically-fabricated qubits (fig. 1). We cooled the chip in a dilution refrigerator and used dispersive readout through half-wave microwave resonators to measure qubit frequencies [39]. We measured the frequencies of 31 qubits to a precision better than 100 kHz using a Ramsey fringe method. The qubit frequencies had random variation $\sigma_f = 132.3$ MHz (fig. 1), or 2.3% of the median frequency. After warming the qubits to room temperature, we measured their junction resistances. In fig. 1, we show a plot of R_n compared to transmon frequency, demonstrating that the observed variation in σ_f is accounted for almost entirely by R_n variation. The behavior may be fit to a power law of approximately $-\frac{1}{2}$ power, as expected from transmon theory and the Ambegaokar-Baratoff formula. For a population of transmon qubits whose frequency scatter is dominated by scatter in R_n , we expect the fractional standard

deviation in R_n to be twice that of σ_f . This is consistent with the standard deviation in junction resistances which is found to be σ_R of 365 Ω , or 4.6% of the median R_n . We also assess the fidelity of the frequencies to the f -vs- R_n correlation in terms of the residual scatter after subtracting the fit line from the frequency values. This appears in the inset in fig. 1 and exhibits a standard deviation 14.5 MHz, or 0.25% of the qubit median frequency.

B. Tuning Using Selective Laser Anneal

To reduce σ_f , we developed a technique for selective laser anneal to shift tunnel resistance R_n by pre-calibrated increments. (See section IV and fig. 2). We demonstrate the achievable frequency control of this technique by shifting the 31 measured qubits into a two-frequency pattern. We employed an R_n vs f correlation (fig. 1) to designate the target resistances. We shifted 16 junctions to one target R_n and 15 to another target R_n . After tuning, the group of 16 junctions had median resistance 7.984 k Ω and the group of 15 had median resistance 8.798 k Ω . The 31 junctions reached their targets with an overall precision of $\sigma_R = 51\Omega$, about 0.61%. In a dilution refrigerator, we re-measured the frequencies of the qubits in the two groups. Aside from two of the qubits, which we measured using CW spectroscopy (precision 2 MHz), all qubits were remeasured in the same way as in the first cooldown. The resulting frequencies appear in fig. 1. The two frequency groups are approximately normally-distributed and have medians $f_{0,1} = 5.430$ GHz and $f_{0,2} = 5.7046$ GHz. Calculating $\sigma_f = \sqrt{\langle (f_i - f_{0,j})^2 \rangle}$, where $f_{0,j}$ represents $f_{0,1}$ or $f_{0,2}$ as appropriate for a given qubit Q_i , we assess the overall precision $\sigma_f = 14.0$ MHz. This imprecision is nearly identical to the residual scatter from the $f(R)$ fit line (fig. 1) which guided the tuning, and the fractional precision $\sigma_f / \langle f \rangle = 0.25\%$ is slightly better than half of the fractional precision in setting R_n . By these comparisons, we see that in this experiment σ_f is limited by both the precision of setting R_n and the precision of predicting f from R_n . Drift in R_n reported in the literature [32] does not appear to be a limiting factor in this study. Achieving smaller σ_f will require improvements in setting R_n . As we show in section IV, the laser-anneal tuning technique is capable of precisions of 0.3% in R_n . On that basis the imprecision of 14.5 MHz in predicting f from R_n would dominate the imprecision in σ_f .

III. DISCUSSION

Our post-fabrication trimming reduced σ_f by 9.5 \times compared to initial fabrication. To assess whether this level of precision is sufficient to reliably prepare lattices of fixed-frequency transmons capable of error-correcting codes, we must quantify the frequency-crowding problem. Transmon qubits are weakly anharmonic and have decreasing transition energies at higher levels.

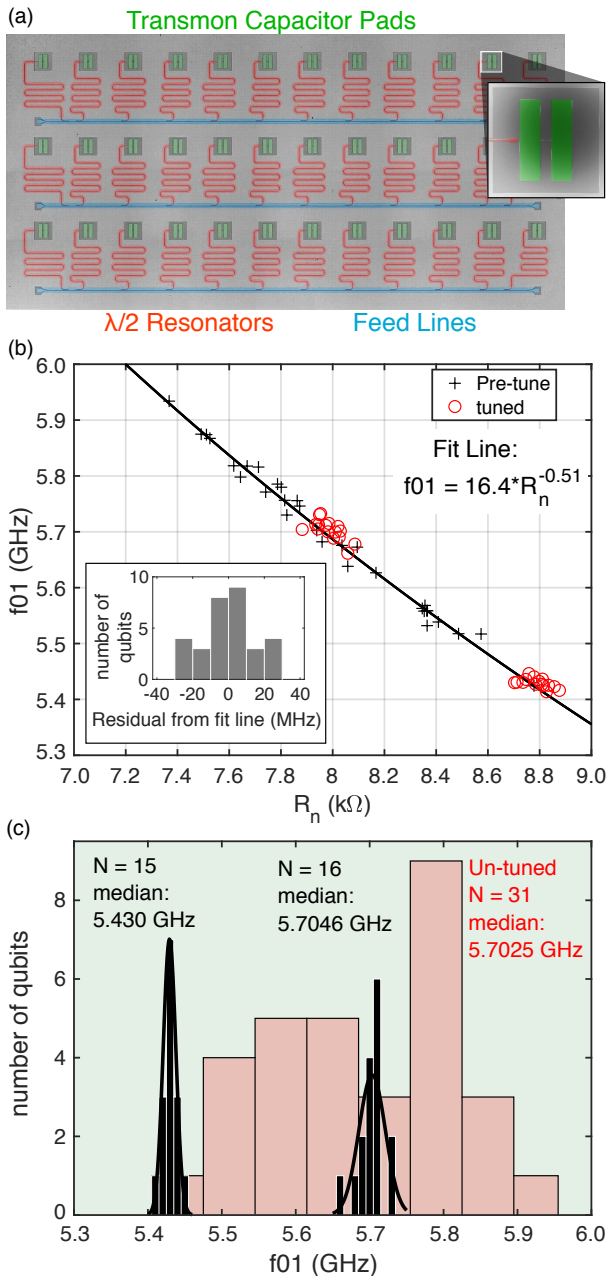


FIG. 1. (a) Chip type used to assess σ_f . False-colored image. 36 fixed-frequency transmon qubits, each including a 500×320 micron planar capacitor and a $\sim 0.1 \times 0.1$ micron Al/AlO_x/Al tunnel junction, are prepared identically on a 20×10 mm Si substrate. A half-wavelength coplanar waveguide resonator at each qubit enables dispersive readout. Resonators are frequency-multiplexed in groups of 12. (b) **Transmon frequency vs R_n .** Power law fit of pre-tuned population. Inset histogram (10 MHz bins) shows residual scatter in frequency relative to fit line. (c) **Distributions of qubit frequencies.** Initial median was 5.7025 GHz and spread $\sigma_f = 132.3$ MHz (red histogram, 70 MHz bins). Using selective laser-anneal (figure 2) we prepared these qubits into two distinct frequency populations with medians 5.430 and 5.7046 GHz. (Black histograms, 10 MHz bins) Each population is outlined by a gaussian curve centered at its local median frequency. Combined spread is $\sigma_f = 14.0$ MHz.

Therefore, degeneracies among the $|0\rangle \rightarrow |1\rangle$, $|1\rangle \rightarrow |2\rangle$ and $|0\rangle \rightarrow |2\rangle$ transitions of nearby qubits can all contribute to ‘frequency collisions.’ We must consider the relative frequencies of both nearest-neighbors and next-nearest-neighbors in the lattice [22, 41, 42]. Fig 3 illustrates the relative positions of nearest-neighbor and next-nearest-neighbor qubits in a section of lattice, and table I lists the seven cases most likely to lead to gate errors [22]. We can think of them qualitatively as follows: Type 1 causes hybridization of states in Q_j and Q_k , while in type 2 the CR pulse excites Q_j into the non-computational $|2\rangle$ state. Type 3 excites Q_k to the $|2\rangle$ state, but does not require a CR tone. In condition 4, ZX is weak, which implies long gate times and increased gate error [22, 23]. In type 5, the CR gate addresses an additional neighboring qubit. In type 6, when one qubit is the target of a CR gate, its next-nearest-neighbor leaks to the $|2\rangle$ state. Type 7 causes Q_j to leak to the $|2\rangle$ state during a CR gate.

Around each of the ‘frequency collisions’ described in table I, we can designate a window of undesired frequencies. This breaks the frequency space into allowed and forbidden regions. Type 4 listed in table I defines forbidden zones where ZX coupling is too low. For the other six conditions, we forbid regions where the ‘frequency collision’ is the dominant source of gate error. Existing multi-qubit systems with CR gates typically exhibit two-qubit gate errors of 1 to 2 % regardless of frequency [12, 41]. Ref [22] considers an effective-Hamiltonian model for the CR gate, as a function of the relative frequency of control and target qubits. We use this model to estimate the frequency windows for nearest-neighbor collisions (table I, types 1 to 3) to cause gate errors exceeding ~ 1 %. We make an assumption that similar bounds apply to next-nearest-neighbor interactions (types 5 to 7).

A useful lattice of qubits should enable high quantum volume and fault-tolerant operation while avoiding all of the ‘frequency collisions’ and forbidden regions presented in table I. Both lattice layout and the pattern of qubit frequencies are relevant. We consider three types of lattices: square, ‘heavy-square’ and ‘heavy-hexagon’ (fig. 3). Lattices comprise qubits and two-qubit connections, each qubit being linked to no more than four neighbors. In many practical implementations, these links comprise microwave-resonant buses. A square lattice facilitates ‘surface code’ fault-tolerant codes [43]. Recent literature describes hybrids of the surface code with Bacon-Shor type codes, which can be employed in ‘heavy hexagon’ and ‘heavy square’ lattices to achieve fault-tolerance, albeit with lower error thresholds than the surface code [30]. In addition to the data and ancilla qubit roles employed in the surface code, these hybrid codes assign a portion of the lattice as ‘flag’ qubits.

In the square lattice, every qubit in the bulk of the lattice lies on a degree-four vertex, while some at edges have degree two or degree three. If we populate the

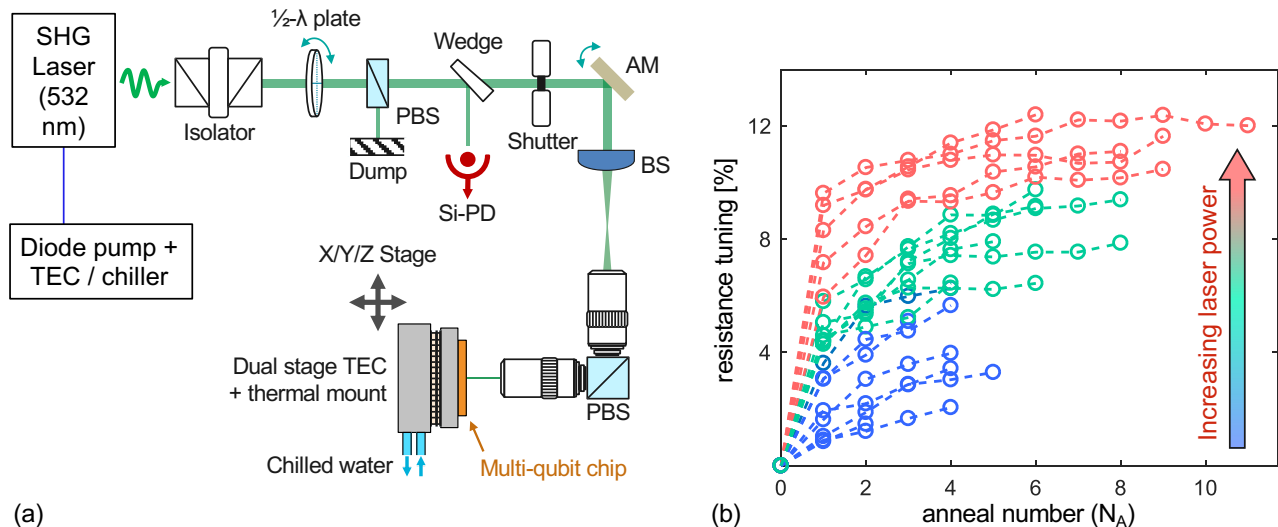


FIG. 2. (a) Schematic of apparatus, “Laser Annealing of Stochastically Impaired Qubits” (LASIQ). A 532 nm (frequency doubled) diode-pumped solid-state laser is used as the laser annealing source. Active power calibration is accomplished via a half-wave plate and PBS combination, with feedback from a Si-PD. A piezoelectric mirror mount actively aligns the beam to the junction center via image pattern recognition. The beam is shaped as necessary to avoid direct illumination of the junction, and beam size is condensed 4× using a dual-objective setup [40]. (b) Iterative anneal demonstration. Adaptive anneal progression towards R_n targets in 20 tunnel junctions. Greater fractional tuning requires greater anneal powers and anneal numbers. Abbreviations: SHG: second harmonic generation, PBS: polarizing beam splitter, Si-PD: silicon photodiode, AM: alignment mirror, BS: beam shaper, TEC: thermoelectric cooler.

Type	Definition	Participants	Bounds
1	$f_{j,01} = f_{k,01}$	Nearest-neighbor qubits Q_j, Q_k	± 17 MHz
2	$f_{j,02} = 2f_{k,01}$	Control qubit Q_j , target qubit Q_k	± 4 MHz
3	$f_{j,01} = f_{k,12}$	Nearest-neighbor qubits Q_j, Q_k	± 30 MHz
4	$f_{k,01} < f_{j,12}$ or $f_{j,01} < f_{k,01}$	Control qubit Q_j , target qubit Q_k	—
5	$f_{i,01} = f_{k,01}$	Q_j is control to Q_i and/or Q_k & is nearest-neighbor to both.	± 17 MHz
6	$f_{i,01} = f_{k,12}$ or $f_{i,12} = f_{k,01}$	Q_j is control to Q_i and/or Q_k & is nearest-neighbor to both.	± 25 MHz
7	$f_{j,02} = f_{k,01} + f_{i,01}$	Q_j is control to Q_i and/or Q_k & is nearest-neighbor to both.	± 17 MHz

TABLE I. Seven most likely types of ‘frequency collision’. For bus-coupled transmon qubits employing cross-resonance gates and having anharmonicity ~ -330 MHz. Relative qubit positions illustrated in inset of fig. 3. Bounds for types 1,2,3 are estimated from model results [22] as the region where gate errors due to ‘frequency collision’ exceed $\sim 1\%$. Bounds for types 5,6,7 are based on those in types 1 and 3.

square lattice with 5 distinct frequencies of qubits, $f_5 > f_4 > f_3 > f_2 > f_1$, with appropriate spacing between the frequencies, we can avoid all the forbidden regions of table I [10]. In fig. 3, we illustrate this pattern for square lattices capable of distance-5 ($d = 5$) rotated surface codes. Condition 4 of table I requires $f_{control} > f_{target}$, so the pattern also fixes the direction of CNOT gate for each pair.

In contrast to the square lattice, the ‘heavy square’ lattice includes both degree-two and degree-four vertices in the bulk. Degree-one, -two or -three vertices appear at the edges. We take advantage of this pattern to make all the degree-two vertices control qubits, using a three-frequency pattern $f_3 > f_2 > f_1$. Since every control qubit (frequency f_3) is linked to at most two target qubits, we need only two properly-chosen target-qubit frequencies (f_1 and f_2) to satisfy conditions 5, 6 and 7

of table I, as shown in fig. 3. A third type of lattice, the ‘heavy hexagon’, uses a similar scheme. Here the bulk of the lattice includes degree-three and degree-two vertices. Additional degree-two and degree-one vertices lie at the edges. In this lattice, all of the ‘frequency collisions’ and forbidden regions can be satisfied using only three frequencies $f_3 > f_2 > f_1$, with all control qubits residing on degree-two vertices with frequency f_3 .

We use a Monte Carlo model to quantify the frequency-crowding in each lattice type. We sample the qubits at random frequencies drawn from normal distributions characterized by σ_f , and count the collisions defined in table I. (See section IV.) In fig. 4, we show the mean number of ‘frequency collisions’ predicted by the Monte Carlo model for each lattice type and frequency pattern, as a function of σ_f . As $\sigma_f \rightarrow 0$, the lattice approaches the ideal patterns of fig. 3, and has zero ‘frequency

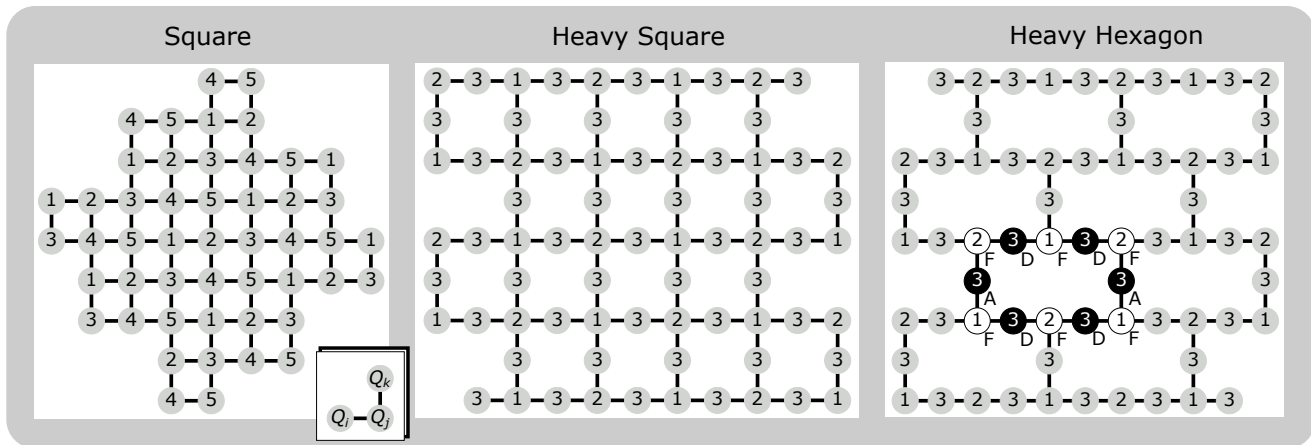


FIG. 3. **Lattice and frequency-pattern examples.** Lattices are capable of $d = 5$ codes. Patterns of qubit frequencies avoid all conditions in table I. Statistical model is applied to these examples and to equivalent lattices at $d = 3$ and $d = 7$. (See Supplementary Figures 1-9.) Square lattice includes 49 qubits in 5-frequency pattern. Heavy-square lattice includes 73 qubits in 3-frequency pattern. Heavy-hexagon lattice includes 65 qubits in 3-frequency pattern. In a portion of the heavy-hexagon lattice, we indicate qubits' intended gate roles: control (black circles) or target (white circles); as well as code roles: data (D), ancilla (A) or flag (F) [30]. Inset shows relative positions of qubits for collision definitions of table I. Q_j is coupled to nearest-neighbors Q_i and to Q_k . Qubits Q_i and Q_k are next-nearest-neighbors.

collisions'. As σ_f increases, the number of 'frequency collisions' rises steadily. As $\sigma_f \rightarrow f_{01} - f_{12}$, the different conditions appearing in table I all become likely, and a limiting number of 'frequency collisions' is reached. Yield follows the inverse trend, as seen in fig. 4. As σ_f increases, the likelihood of finding a 'collision free' chip falls off sharply. While the step sizes between frequencies f_1 to f_5 are important, absolute frequency values are not. Setting $f_1 = 5.0$, $f_2 = 5.07$ and $f_3 = 5.14$ GHz works as well as $f_1 = 5.05$, $f_2 = 5.12$ and $f_3 = 5.19$ GHz.

The yield and mean collision number are a function of the several different collision types and bounds, so they are not readily susceptible to an analytic formulation. However, we can propose a simplified model for yield: in order for a lattice to be collision-free, every qubit in the lattice must fall within some frequency 'window' $\pm \Delta f$ relative to its setpoint. Presuming the qubit frequencies are normally distributed, the probability of this occurring goes as the cumulative distribution function, raised to the power N , where N is the number of qubits: $\left[\int_{-\infty}^{(\Delta f / \sigma_f)} e^{-\frac{1}{2}x^2} dx \right]^N$. In the yield plot in fig. 4, we fit this expression to find Δf for each lattice.

These model results allow us to predict how different lattice types and frequency patterns will respond to fabrication imprecision. As shown in fig. 4, if imprecision σ_f is greater than 30 MHz, any $d = 5$ lattice will exhibit > 10 'frequency collisions' of one or another of the types listed in table I, causing the affected gates to have error rates above $\sim 1\%$. However, if $\sigma_f = 10$ MHz then on average the $d = 5$ square lattice will exhibit 5 'frequency collisions', while the 'heavy square' and 'heavy hexagon' lattices will exhibit 0.1 'frequency collision'. Considered in terms of yield, we see from fig. 4

that if $\sigma_f = 10$ MHz, then for a $d = 5$ device, a square lattice with 5-frequency pattern has a 0.8% likelihood to be 'collision free', whereas a 'heavy square' lattice with 3-frequency pattern has 90% likelihood and 'heavy hexagon' with 3-frequency pattern has 92% likelihood. Alternatively we can ask, how well do we have to control σ_f ? If we seek a 10% yield, then fig. 4 indicates that for a $d = 5$ device, a square lattice with 5-frequency pattern requires $\sigma_f < 8$ MHz, whereas a 'heavy square' lattice with 3-frequency pattern requires $\sigma_f = 16$ MHz and 'heavy hexagon' with 3-frequency pattern requires $\sigma_f = 17$ MHz. Although the square lattice requires 10 to 20 % fewer qubits than the other types at each distance d , it requires far better frequency precision.

The as-fabricated σ_f seen in fig. 1 is 132.3 MHz. (See section II) The Monte Carlo modeling finds that for a heavy-hexagon lattice at $d = 3$ scale this σ_f can enable 0.1% yield of collision-free chips. Other lattice types and larger scales will all have yield $\ll 0.1\%$. The re-tuned $\sigma_f = 14.0$ MHz demonstrated in fig. 1 will improve the yield in all types of lattice. Predictions of the Monte Carlo model for $\sigma_f = 14.0$ MHz appear in table II. At $d = 5$ scale the heavy-hexagon and heavy-square lattices and 3-frequency patterns should be collision-free nearly one-third of the time, while at $d = 7$ scale the yield is about four times smaller, still reasonable for prototype systems.

As seen from the Monte Carlo analysis, the laser-anneal rework method can scale to the > 100 qubit size, enabling a well-chosen lattice and frequency pattern to implement $d = 7$ error-correction codes free of frequency-crowding. To examine needs for the next generation of chips up to the 1000-qubit level, we can coarsely estimate requirements by extrapolating the fixed window model for the

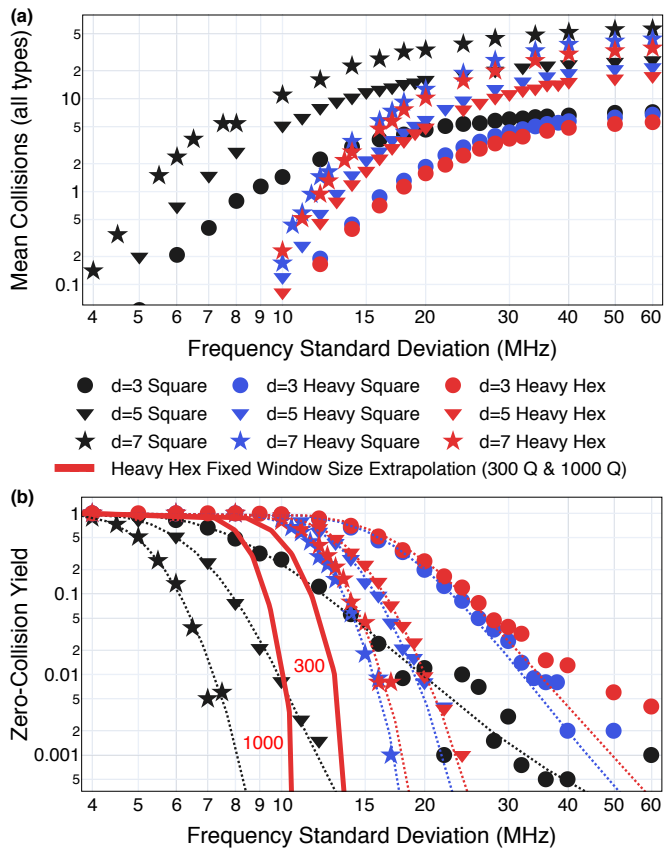


FIG. 4. **Frequency-crowding trends as a function of σ_f .** Results of Monte Carlo simulation. (See section IV.) (a) **Average number of collisions.** and (b) **Fraction of cases having zero ‘frequency collisions’.** Simulation was applied to the lattices and frequency patterns shown in fig. 3, capable of distance-5 codes, as well as to $d = 3$ and $d = 7$ scale lattices of square, heavy-square or heavy-hexagon type. (See Supplementary Figures 1-9 for lattice layouts and table II for numbers of qubits.) Color-coded dotted lines in part (b) are fits of each lattice yield to expression $\left[\int_{-\infty}^{\Delta f / \sigma_f} e^{-\frac{1}{2}x^2} dx \right]^N$, where N is the number of qubits and $\pm \Delta f$ defines an allowable ‘window’ around frequency set-points. (See table II.) Using this expression, two solid red lines predict yield for the heavy-hexagon lattice type at 300 and 1000 qubits, using $\Delta f = 27.99$ and 26.32 MHz, respectively. See fig. 5 for estimation of Δf as a function of qubit number.

heavy-hexagon lattice as shown in fig. 5. While the $\sigma_f = 14.0$ MHz demonstrated here enables practical yield up to the 100 to 200 qubit scale, it is clear that roughly a factor of two further improvement is needed to scale towards 1000 qubits. Since this precision is also better than the resistance-to-frequency prediction precision shown in this work, development of further refinements in tuning and frequency prediction approaches will be necessary as the scale of fixed-frequency transmon circuits surpass the 100 qubit milestone.

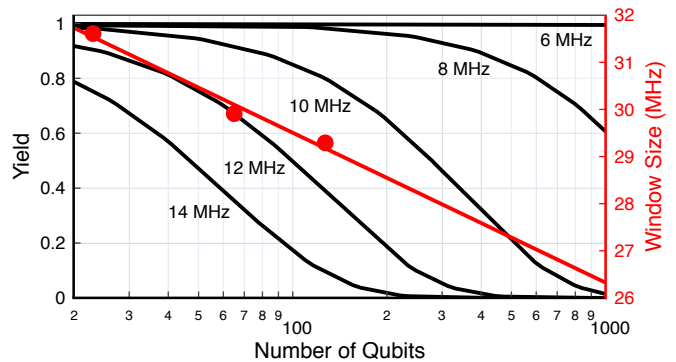


FIG. 5. **Yield scaling for heavy hexagon lattice.** Fixed window size model. (left axis) Model yields for σ_f ranging from the 14 MHz demonstrated in this work to 6 MHz that would optimize future scaling yield beyond the 1000Q level. (right axis) Fixed window size fits to the $d=3$, $d=5$ and $d=7$ heavy hexagon lattice, as well as a fit of these values to expression $A + B \cdot \log(N_{QB})$, extrapolated from 20 to 1000 qubits. This trend illustrates varying frequency crowding constraints as a function of lattice size.

IV. METHODS

A. Chip Fabrication

A chip of the kind used to determine σ_f and to test our laser-anneal rework process appears in fig. 1. All microwave elements comprise Nb films ~ 200 nm thick on a silicon substrate. Each qubit is coupled to a readout resonator but is not directly coupled to any nearby qubits. All transmon capacitors are identical. Junctions are fabricated using identical electron-beam lithographic patterns and deposited simultaneously using double-angle deposition and oxidation [44]. The individual qubit design is similar to that used in Ref [21] with aharmonicity $f_{12} - f_{01} \simeq -330$ MHz. Junctions have linear dimension ~ 100 nm and are designed for I_c of ~ 30 nA. During packaging, we accidentally damaged three of the 36 qubits and found these to be non-functional when cooled in a dilution refrigerator. We left two of the remaining 33 qubits un-tuned as experimental controls, so that our tuning demonstration includes 31 qubits.

B. Tuning Using Selective Laser Anneal

We have built an integrated junction rework system that can measure and modify the junction resistance. Fig. 2 shows a schematic of our laser annealing system, which we call ‘‘Laser Annealing of Stochastically Impaired Qubits’’ (LASIQ). The laser output is generated by a diode-pumped solid-state laser, frequency doubled to 532 nm. Active power control of the anneal beam is performed using a piezo-rotary mounted waveplate and polarizing beam splitter (PBS), which is adaptively adjusted based on a pick-off beam measured on a downstream silicon photodiode. A precision-timed shutter is

Lattice & frequency pattern	Code distance	Qubits	$\sigma_f = 132.3$ MHz		$\sigma_f = 14$ MHz		Δf Window (MHz)
			Mean number of collisions	Yield of collision-free devices	Mean number of collisions	Yield of collision-free devices	
Square, 5-frequency	$d = 3$	17	9	$\ll 0.1\%$	3	6%	13.96
	$d = 5$	49	35	$\ll 0.1\%$	10	$< 0.1\%$	13.23
	$d = 7$	97	78	$\ll 0.1\%$	23	$\ll 0.1\%$	12.12
Heavy square, 3-frequency	$d = 3$	25	10	$\ll 0.1\%$	0.4	67%	30.89
	$d = 5$	73	33	$\ll 0.1\%$	1.5	27%	29.49
	$d = 7$	145	70	$\ll 0.1\%$	3.5	6%	29.06
Heavy hexagon, 3-frequency	$d = 3$	23	8	0.1%	0.4	70%	31.61
	$d = 5$	65	25	$\ll 0.1\%$	1.2	33%	29.91
	$d = 7$	127	51	$\ll 0.1\%$	2.7	8%	29.29

TABLE II. **Monte-Carlo model predictions of mean number of collisions and yield of collision-free chips.** Full results of Monte-Carlo model of frequency-crowding appear in fig. 4. Here we show values for as-fabricated precision $\sigma_f = 132.3$ MHz, and for demonstrated frequency precision of the laser-anneal method, $\sigma_f = 14$ MHz. (fig. 1) in different lattices and frequency patterns (fig. 3 and Supplementary Figures 1-9). The Δf values correspond to the fit lines in fig. 4: in order for the device to be collision-free, every qubit in the lattice must fall within \pm this ‘window’, relative to its set-point.

used to control the anneal duration, and beam alignment is performed using a mechanical mirror mount which directs the beam via pattern recognition to the transmon junction center. The beam is shaped as needed to avoid illuminating the junction directly [40].

By careful control of laser power and pulse duration, we use this system to adjust R_n . This process overcomes the imprecision due to transmon fabrication, with a residual imprecision σ_f due to the rework process. To develop the process, we prepared a set of more than 150 junctions identically to qubit junctions, and measured their response to a range of laser powers and exposure times. We recorded R_n shifts up to 15% relative to initial R_n , for anneal durations varying by an order of magnitude and laser powers varying by 20%. Response to laser power in particular was highly nonlinear. Based on these empirical calibrations of R_n shift to power and exposure, we established a qubit tuning process: We first measure the transmon junction’s R_n using four-point probing of the transmon capacitor pads at 25 °C. Using a $f(R_n)$ prediction based on a previously determined correlation curve (fig. 1), we assign the junction a target resistance corresponding to the target frequency in a multiqubit chip lattice. Because the anneal can shift R_n in only one direction, the target must be higher than the initial R_n . We anneal the qubit junction using laser power and duration chosen from our calibration set, then re-measure its R_n . A junction requiring large shifts in R_n may require repeated anneals to reach its target, as shown in fig. 2. The control algorithm increases the resistance until the measured value is within 0.3% of the target value. In a separate trial of tuning precision, more than 300 junctions were tuned to target R_n s ranging from 0.4% to 14.5% above their initial values, and landed successfully within this 0.3% margin. We expect 0.3% imprecision in R_n to introduce 0.15% imprecision in transmon frequency.

C. Monte Carlo Frequency-Crowding Model

Using a Monte Carlo model, we can estimate the incidence of ‘frequency collisions’ in a lattice as a function of σ_f . We assume that imperfect frequency-setting will distribute qubit frequencies normally around their design frequencies with standard deviation σ_f . For lattices of the type shown in fig. 3, we designate 3 to 5 frequencies f_1, f_2, f_3, f_4, f_5 spaced at regular intervals in the pattern shown. We set $f_1 = 5$ GHz, similar to real-world transmons [38, 45]. We sample the qubit frequencies randomly around these values and count the collisions throughout the lattice, as listed in table I. This process is illustrated in fig. 6. We repeat the frequency-assignment and counting to build statistics for a given lattice and frequency pattern. We then repeat the model for a range of σ_f values from 0 to 150 MHz. We repeat the entire process over a range of frequency spacings, to find the spacing that minimizes ‘frequency collisions’ at each value of σ_f . As a function of σ_f we can then extract 1) the mean number of total collisions in the lattice, and 2) the fraction of repetitions which result in zero collisions (‘yield’). Our simulations used 1000 repetitions except to find yield below 1% in $d = 5$ lattices and below 0.2% in $d = 3$ lattices, which used 4000 repetitions, and in $d = 7$ lattices to find mean collisions for $\sigma_f < 16$ MHz or yield above 50% (100 repetitions) or to find mean collisions for $\sigma_f > 16$ MHz (40 repetitions).

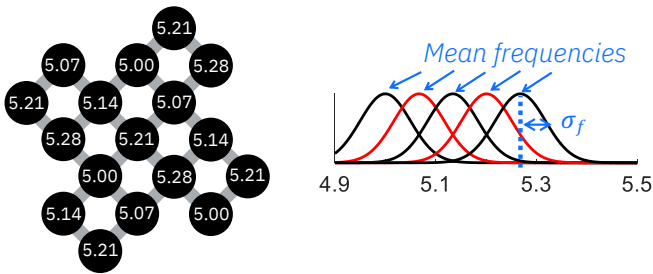


FIG. 6. **Frequency collision statistical model.** **Left:** Square lattice, $d = 3$ with 5-frequency pattern of fig. 3: $f_1 = 5.00$, $f_2 = 5.07$, $f_3 = 5.14$, $f_4 = 5.21$, $f_5 = 5.28$ GHz. To model the lattice statistically, treat the frequencies f_1 to f_5 as means of distributions. **Right:** Mean frequencies and normal distributions characterized by σ_f . For each position in the lattice, sample from the local distribution. Choose random frequencies in this fashion, count collisions as described in table I and repeat to gather statistical sample. Process is repeated for differing spacings between mean frequencies f_1 to f_5 , and for different distribution widths σ_f .

-
- [1] Kandala, A. *et al.* Hardware-efficient variational quantum eigensolver for small molecules and quantum magnets. *Nature* **549**, 242–246 (2017).
- [2] Havlíček, V. *et al.* Supervised learning with quantum-enhanced feature spaces. *Nature* **567**, 209–212 (2019).
- [3] Hempel, C. *et al.* Quantum Chemistry Calculations on a Trapped-Ion Quantum Simulator. *Phys. Rev. X* **8**, 031022 (2018).
- [4] Colless, J. *et al.* Computation of Molecular Spectra on a Quantum Processor with an Error-Resilient Algorithm. *Phys. Rev. X* **8**, 011021 (2018).
- [5] Nam, Y. *et al.* Ground-state energy estimation of the water molecule on a trapped-ion quantum computer. *npj Quantum Inf.* **6**, 1–6 (2020).
- [6] Kandala, A. *et al.* Error mitigation extends the computational reach of a noisy quantum processor. *Nature* **567**, 491–495 (2019).
- [7] Córcoles, A. D. *et al.* Challenges and Opportunities of Near-Term Quantum Computing Systems. *Proc. IEEE* **107**, 1–15 (2019).
- [8] Chow, J. M. *et al.* Implementing a strand of a scalable fault-tolerant quantum computing fabric. *Nat. Comm.* **5**, 4015 (2014).
- [9] Córcoles, A. *et al.* Demonstration of a quantum error detection code using a square lattice of four superconducting qubits. *Nat. Comm.* **6**, 6979 (2015).
- [10] Gambetta, J. M., Chow, J. M. & Steffen, M. Building logical qubits in a superconducting quantum computing system. *npj Quantum Inf.* **3**, 2 (2017).
- [11] Takita, M. *et al.* Demonstration of weight-four parity measurements in the surface code architecture. *Phys. Rev. Lett.* **117**, 210505 (2016).
- [12] Takita, M., Cross, A. W., Córcoles, A. D., Chow, J. M. & Gambetta, J. M. Experimental demonstration of fault-tolerant state preparation with superconducting qubits. *Phys. Rev. Lett.* **119**, 180501 (2017).
- [13] Kelly, J. *et al.* State preservation by repetitive error detection in a superconducting quantum circuit. *Nature* **519**, 66–69 (2015).
- [14] Risté, D. *et al.* Detecting bit-flip errors in a logical qubit using stabilizer measurements. *Nat. Comm.* **6**, 6983 (2015).
- [15] Ofek, N. *et al.* Extending the lifetime of a quantum bit with error correction in superconducting circuits. *Nature* **536**, 441–445 (2016).
- [16] Cross, A. W., Bishop, L. S., Sheldon, S., Nation, P. D. & Gambetta, J. M. Validating quantum computers using randomized model circuits. *Phys. Rev. A* **100**, 032328 (2019).
- [17] Chow, J. M. *et al.* Simple All-Microwave Entangling Gate for Fixed-Frequency Superconducting Qubits. *Phys. Rev. Lett.* **107**, 080502 (2011).
- [18] Chow, J. M. *et al.* Universal Quantum Gate Set Approaching Fault-Tolerant Thresholds with Superconducting Qubits. *Phys. Rev. Lett.* **109**, 060501 (2012).
- [19] de Groot, P. C. *et al.* Selective darkening of degenerate transitions for implementing quantum controlled-NOT gates. *New J. Phys.* **14**, 073038 (2012).
- [20] Rigetti, C. & Devoret, M. Fully microwave-tunable universal gates in superconducting qubits with linear couplings and fixed transition frequencies. *Phys. Rev. B* **81**, 134507 (2010).
- [21] Sheldon, S., Magesan, E., Chow, J. M. & Gambetta, J. M. Procedure for systematically tuning up crosstalk in the cross resonance gate. *Phys. Rev. A* **93**, 060302 (2016).
- [22] Magesan, E. & Gambetta, J. M. Effective Hamiltonian models of the cross-resonance gate. *Phys. Rev. A* **101**, 052308 (2020).
- [23] Ware, M. *et al.* Cross-resonance interactions between superconducting qubits with variable detuning (2019).

- Preprint at <http://arxiv.org/abs/1905.11480v1>.
- [24] Koch, J. *et al.* Charge-insensitive qubit design derived from the Cooper pair box. *Phys. Rev. A* **76**, 042319 (2007).
- [25] Potts, A., Parker, G., Baumberg, J. & de Groot, P. CMOS compatible fabrication methods for submicron Josephson junction qubits. *IEE Proc.: Sci. Meas. Technol.* **148**, 225–228 (2001).
- [26] Wu, X. *et al.* Overlap junctions for high coherence superconducting qubits. *Appl. Phys. Lett.* **111**, 032602 (2017).
- [27] Costache, M. V., Bridoux, G., Neumann, I. & Valenzuela, S. O. Lateral metallic devices made by a multiangle shadow evaporation technique. *J. Vac. Sci. Technol., B* **30**, 04E105 (2012).
- [28] Kreikebaum, J. M., O’Brien, K. P., Morvan, A. & Siddiqi, I. Improving wafer-scale Josephson junction resistance variation in superconducting quantum coherent circuits. *Supercond. Sci. Technol.* **33**, 06LT02 (2020).
- [29] Ambegaokar, V. & Baratoff, A. Tunneling Between Superconductors. *Phys. Rev. Lett.* **10**, 486–489 (1963).
- [30] Chamberland, C., Zhu, G., Yoder, T. J., Hertzberg, J. B. & Cross, A. W. Topological and Subsystem Codes on Low-Degree Graphs with Flag Qubits. *Phys. Rev. X* **10**, 011022 (2020).
- [31] Chow, J. M., Magesan, E., Steffen, M., Gambetta, J. M. & Takita, M. United States Patent (Pending): US20200161529A1 - Reducing qubit frequency collisions through lattice design (2020).
- [32] Koppinen, P. J., Vist, L. M. & Maasilta, I. J. Complete stabilization and improvement of the characteristics of tunnel junctions by thermal annealing. *Appl. Phys. Lett.* **90**, 053503 (2007).
- [33] Granata, C. *et al.* Trimming of critical current in niobium Josephson devices by laser annealing. *J. Phys.: Conference Series* **97**, 012110 (2008).
- [34] Muthusubramanian, N. *et al.* Local trimming of transmon qubit frequency by laser annealing of Josephson junctions (2019). American Physical Society March Meeting, B29.015.
- [35] Oliva, A. & Monaco, R. Annealing properties of high quality Nb/Al-AlO_x/Nb tunnel junctions. *IEEE Trans. Appl. Supercond.* **4**, 25–32 (1994).
- [36] Lehnert, T., Billon, D., Grassl, C. & Gundlach, K. H. Thermal annealing properties of NbAl/AlO_xNb tunnel junctions. *J. Appl. Phys.* **72**, 3165–3168 (1992).
- [37] Orcutt, J. S. & Rosenblatt, S. United States Patent: 10418540 - Adjustment of qubit frequency through annealing (2019).
- [38] Jurcevic, P. *et al.* Demonstration of quantum volume 64 on a superconducting quantum computing system (2020). Preprint at <https://arxiv.org/abs/2008.08571>.
- [39] Blais, A., Huang, R.-S., Wallraff, A., Girvin, S. M. & Schoelkopf, R. J. Cavity quantum electrodynamics for superconducting electrical circuits: An architecture for quantum computation. *Phys. Rev. A* **69**, 062320 (2004).
- [40] Rosenblatt, S. & Orcutt, J. S. United States Patent: 10170681B1 - laser annealing of qubits with structured illumination (2019).
- [41] McKay, D. C., Sheldon, S., Smolin, J. A., Chow, J. M. & Gambetta, J. M. Three-Qubit Randomized Benchmarking. *Phys. Rev. Lett.* **122**, 200502 (2019).
- [42] Malekakhlagh, M., Magesan, E. & McKay, D. C. First-principles analysis of cross-resonance gate operation (2020). Preprint at <http://arxiv.org/abs/2005.00133>.
- [43] Fowler, A. G., Mariantoni, M., Martinis, J. M. & Cleland, A. N. Surface codes: Towards practical large-scale quantum computation. *Phys. Rev. A* **86**, 032324 (2012).
- [44] Dolan, G. J. Offset masks for liftoff photoprocessing. *Appl. Phys. Lett.* **31**, 337–339 (1977).
- [45] Sheldon, S. *et al.* Characterizing errors on qubit operations via iterative randomized benchmarking. *Phys. Rev. A* **93**, 012301 (2016).

ACKNOWLEDGEMENTS

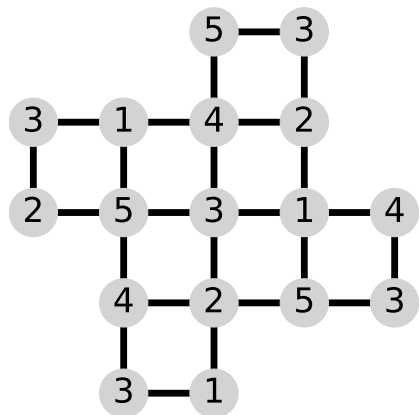
We acknowledge funding from the Intelligence Advanced Research Projects Activity (IARPA) under contract W911NF-16-1-0114, for the multi-qubit test vehicle and frequency-vs-resistance correlation studies. We thank N. Bronn, M. Carroll, C. Chamberland, A. Cross, J. Gambetta, J. Ku, M. Malekakhlagh, D. McKay, B. Plourde, E. Pritchett, A. Rosenbluth, M. Takita, J. Timmerwilch and G. Zhu for helpful discussions. We thank E. Porter for coding assistance, Y. Martin and R. Haight for assistance in constructing the laser optics, and R. Patel for photomicroscopy.

**SUPPLEMENTARY INFORMATION for
Laser annealing Josephson junctions for yielding scaled-up superconducting quantum
processors)**

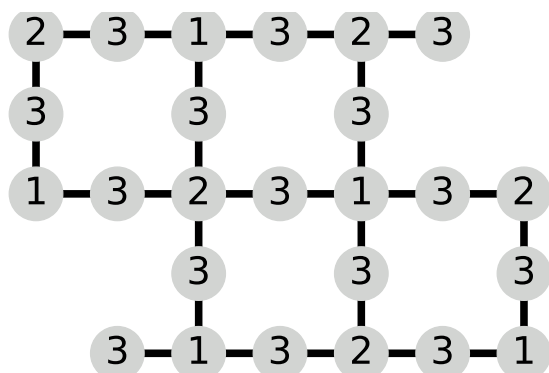
Jared B. Hertzberg, Eric J. Zhang, Sami Rosenblatt, Easwar Magesan, John A. Smolin, Jeng-Bang
Yau, Vivekananda P. Adiga, Martin Sandberg, Markus Brink, Jerry M. Chow, and Jason S. Orcutt
IBM Quantum, IBM T.J. Watson Research Center, Yorktown Heights, NY 10598, USA

(Dated: September 3, 2020)

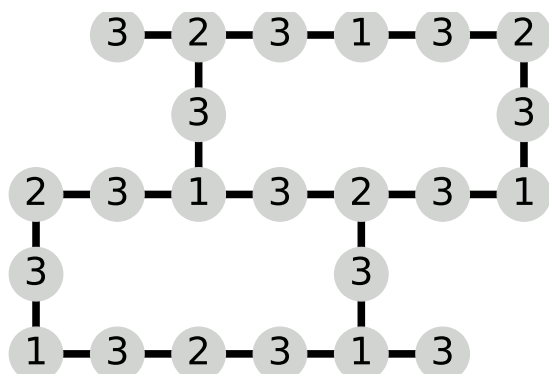
arXiv:2009.00781v4 [quant-ph] 23 Sep 2020



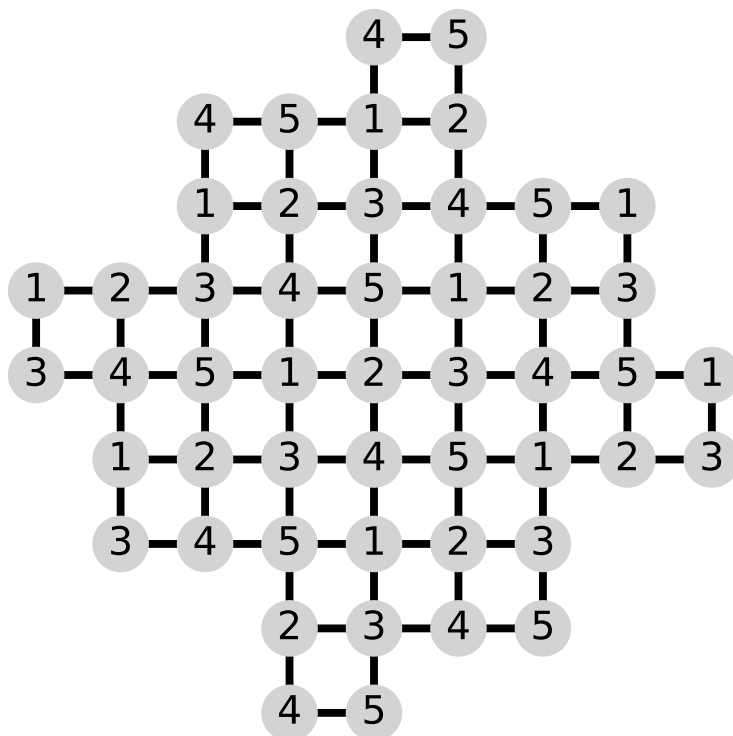
Supplementary Figure 1. Distance-3 square lattice, 17 qubits, 5-frequency pattern



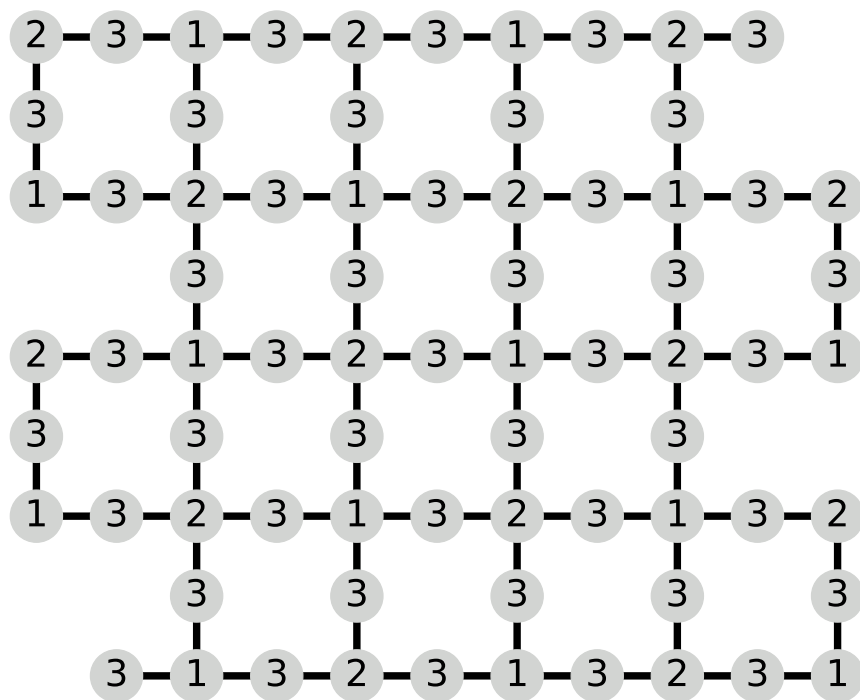
Supplementary Figure 2. Distance-3 heavy-square lattice, 25 qubits, 3-frequency pattern



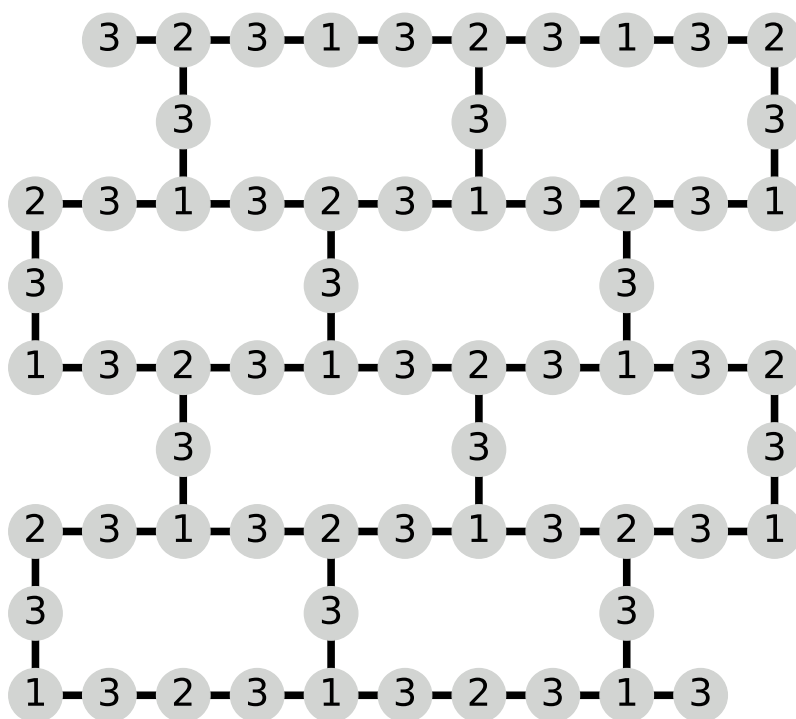
Supplementary Figure 3. Distance-3 heavy-hexagon lattice, 23 qubits, 3-frequency pattern



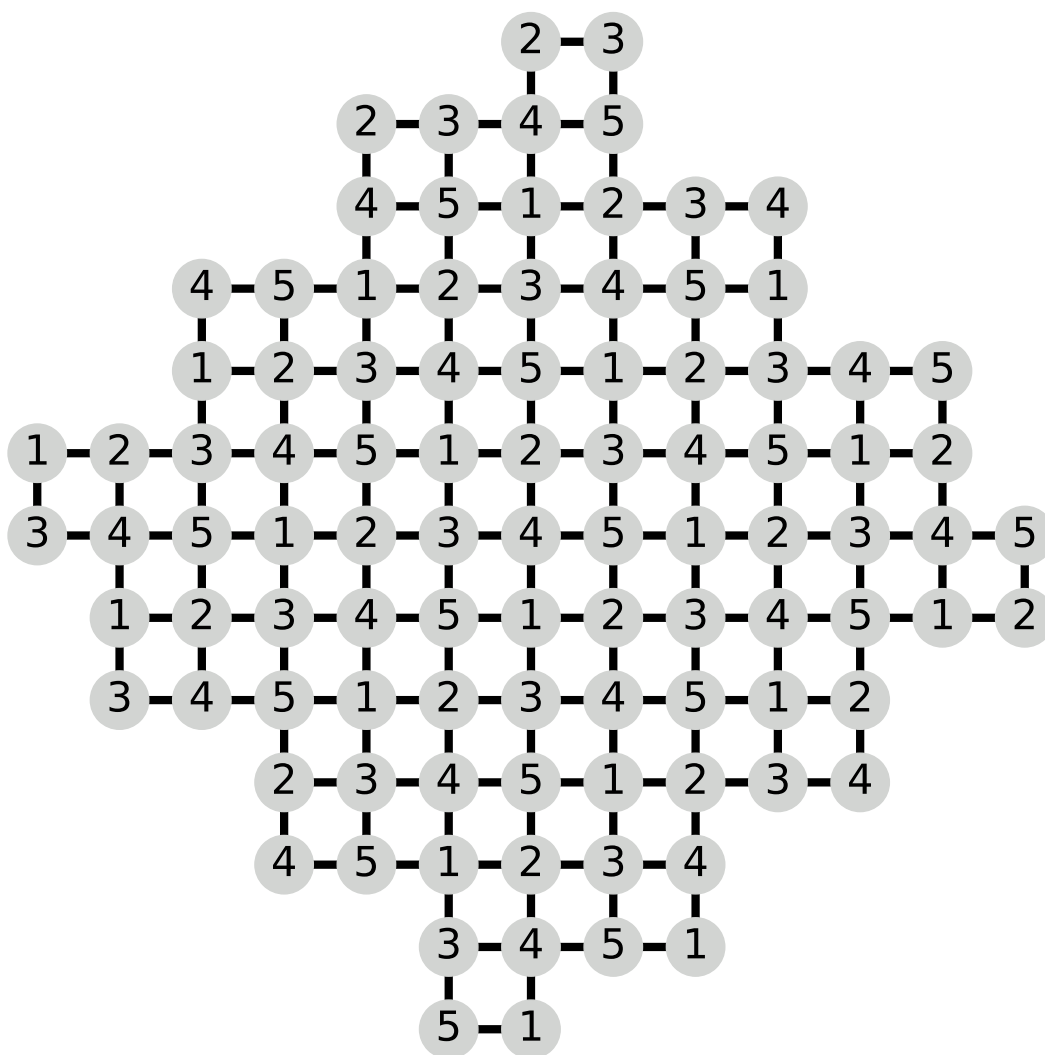
Supplementary Figure 4. Distance-5 square lattice, 49 qubits, 5-frequency pattern



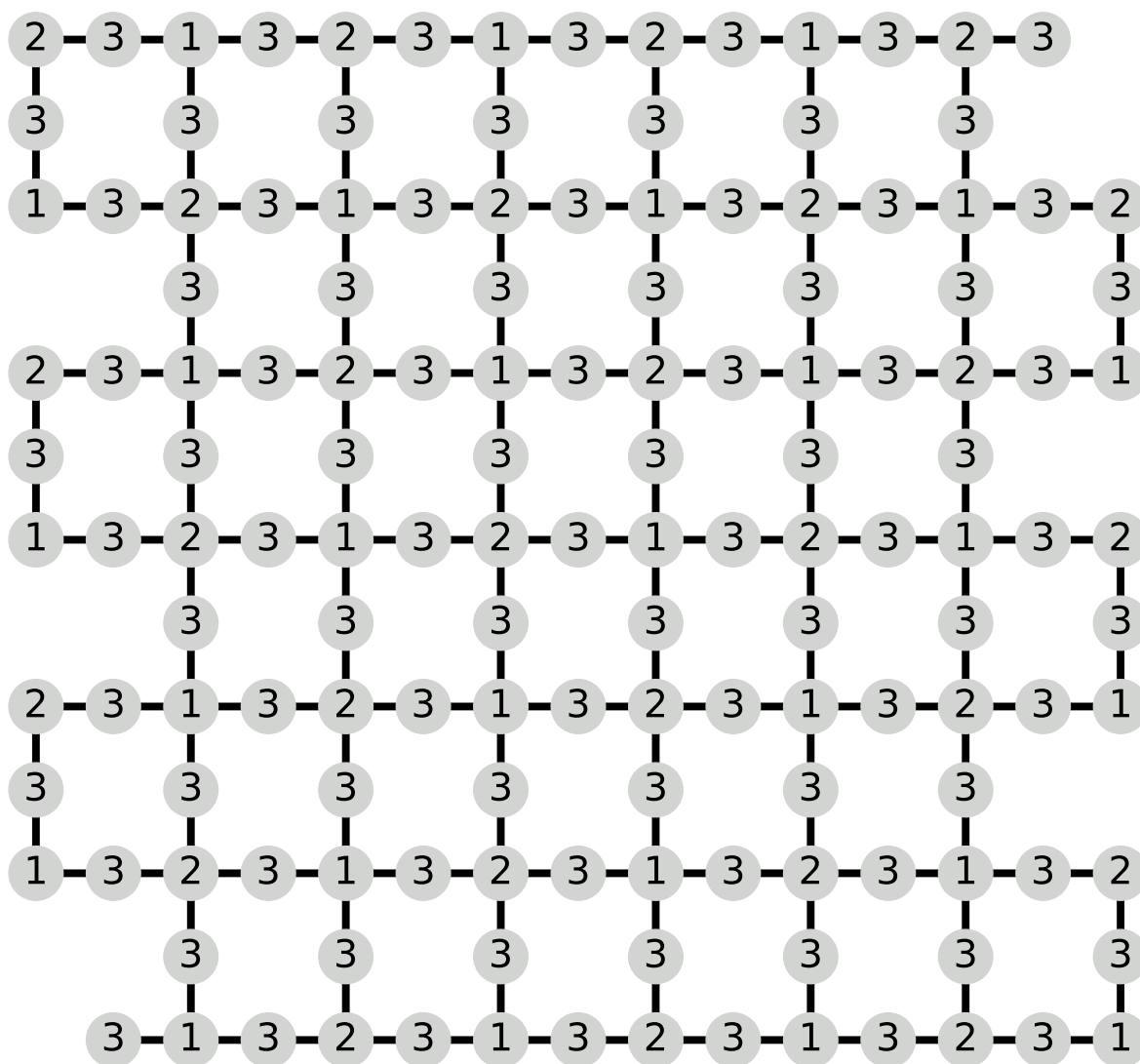
Supplementary Figure 5. Distance-5 heavy-square lattice, 73 qubits, 3-frequency pattern



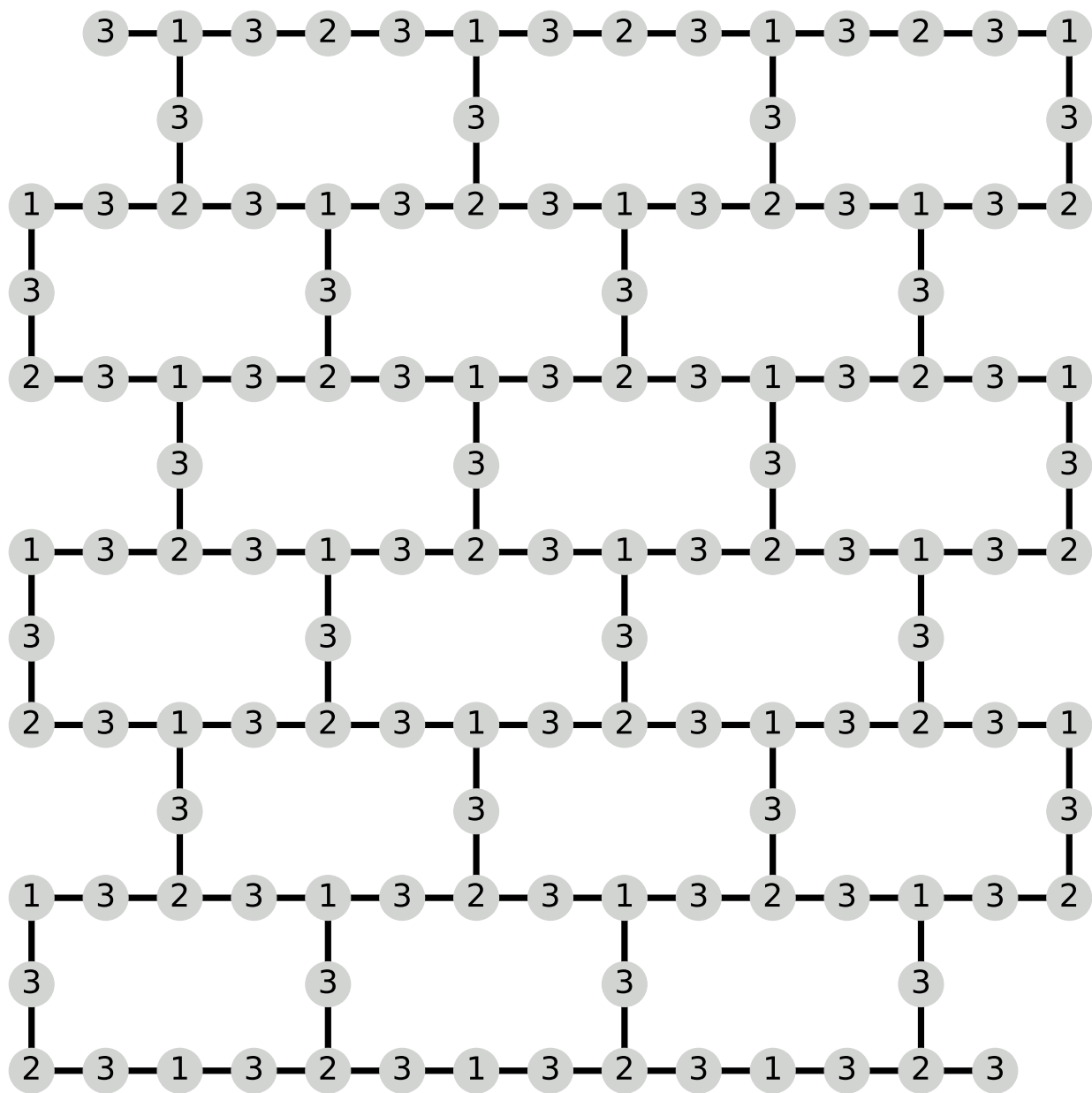
Supplementary Figure 6. Distance-5 heavy-hexagon lattice, 65 qubits, 3-frequency pattern



Supplementary Figure 7. Distance-7 square lattice, 97 qubits, 5-frequency pattern



Supplementary Figure 8. Distance-7 heavy-square lattice, 145 qubits, 3-frequency pattern



Supplementary Figure 9. Distance-7 heavy-hexagon lattice, 127 qubits, 3-frequency pattern